

## Supplementary methods

### Details of MRI acquisition

T1-weighted anatomical data were acquired using an MPRAGE sequence with TR 2300 ms, TE 3.06 ms, FOV 256 mm, voxel size  $1 \times 1 \times 1 \text{ mm}^3$ , flip angle  $9^\circ$ , TI 850 ms, 2-fold in-plane undersampling with GRAPPA (1) and phase-encoding direction anterior to posterior (A>>P).

Multi-shell diffusion-weighted MRI data were acquired using a single-shot spin-echo, echo-planar imaging sequence with dynamic field correction. Data were acquired in the A>>P phase-encoding direction using two b shells ( $30 \times b = 1200 \text{ s/mm}^2$  and  $60 \times b = 2400 \text{ s/mm}^2$ ) applied using a monopolar diffusion scheme, in addition to  $1 \times b = 0 \text{ s/mm}^2$  ( $b_0$ ) image (no diffusion encoding) at the start of acquisition and  $5 \times b = 0 \text{ s/mm}^2$  images at the end. Data acquisition details were as follows: TR 9400 ms, TE 70 ms, FOV 256 mm, voxel size  $2 \times 2 \times 2 \text{ mm}$ , with 2-fold in-plane undersampling.

Optimised quantitative magnetization transfer (qMT) (2) data were acquired on a Siemens Prisma 3T scanner, using a method similar to that described by Cercignani *et al.* (3). QMT data included 11 magnetization transfer (MT)-weighted images with flip angle ( $^\circ$ )/frequency offset (Hz) combinations of: 332/1000; 333/1000; 628/12060; 628/47180; 332/56360; 628/2750;  $2 \times 628/1000$ ; 628/2768; 628/2790; 628/2890; and 1 non-MT-weighted image (4). All data were acquired using the following parameters: TR 32 ms; TE 2.46 ms; phase-encoding direction A>>P, FOV 240 mm, voxel size  $2.5 \times 2.5 \times 2.5 \text{ mm}$ , 64 slices, with 2-fold in-plane undersampling. In addition, three non-MT-weighted images were acquired, with the same parameters as above, but with flip angles of  $3^\circ$ ,  $15^\circ$  and  $7^\circ$ . To account for inhomogeneities in the magnetic field, B0 and B1 maps were also acquired. B0 data were acquired using a gradient echo sequence with TR 330 ms, TE<sub>1</sub> 4.92 ms, TE<sub>2</sub> 7.38 ms, phase-encoding direction A>>P, FOV 240 mm, voxel size  $2.5 \times 2.5 \times 2.5 \text{ mm}$ , and 64 slices. Two B1 images with flip angles of  $120^\circ$  and  $60^\circ$  were acquired using a turbo spin echo sequence with TR 4370 ms, TE 93 ms, phase-encoding direction A>>P, FOV 320 mm, voxel size  $2.5 \times 2.5 \times 2.5 \text{ mm}$ , and 64 slices.

### Details of qMT data preprocessing

Prior to processing, imaging data were reoriented to standard imaging orientation using the FMRIB Software Library (FSL version 6.0.5) (5). Non-brain tissue was then removed from B1, B0, and non-magnetization transfer (no-MT)-weighted images using HD-BET (6). B1 images were corrected for field inhomogeneities using bias field correction in Advanced Normalization Tools (ANTs) (7), after which B1 images were registered together, smoothed and used to create a B1 field map using the double angle method (8). The B1 map was then registered to the  $3^\circ$  flip angle no-MT image using FSL's linear registration tool (FLIRT) (9, 10), after which the registered B1 map as well as the  $3^\circ$ ,  $15^\circ$  and  $7^\circ$  flip angle no-MT images were used to create a T1 map (11) for registration of the qMT data. In addition to the B1 field map, a B0 field map was created in FSL then converted to Hertz and registered to the  $3^\circ$  flip angle no-MT image using non-linear registration in FSL.

All MT data were rigidly aligned to the no-MT image and merged to create a single 4-dimensional qMT image file. Merged qMT data were then registered to the first (no-MT) image using FSL's motion correction registration tool (mcflirt) (10). The merged qMT data were then registered to the T1 map, initialised using an affine matrix of the transformation between the brain-extracted no-MT image and T1 map. The T1-registered, brain-extracted no-MT image was then used to mask the merged qMT data, which was eroded to ensure removal of all non-brain data. The registered, brain-extracted no-MT image was used to estimate a bias field using FMRIB's Automated Segmentation Tool (12), which was then used to perform bias field correction on the registered, brain-extracted, merged qMT data.

Table S1. Effects of maternal thyroid stimulating hormone (TSH) and free thyroxine (FT4) on white matter tissue microstructure. CC: corpus callosum; CG: cingulum; ILF: inferior longitudinal fasciculus; SLF: superior longitudinal fasciculus. P values are uncorrected for multiple comparisons.

Measurement	Microstructural metric	Tract	Spearman's rho	P value
TSH	Fractional anisotropy	CC	-0.040	0.745
		CG	-0.007	0.956
		ILF	0.022	0.856
		SLF	-0.186	0.124
	Mean diffusivity	CC	0.143	0.265
		CG	0.131	0.320
		ILF	<b>0.310</b>	<b>0.015</b>
		SLF	0.183	0.158
	Radial diffusivity	CC	0.114	0.376
		CG	0.156	0.223
		ILF	0.160	0.210
		SLF	0.234	0.065
	Bound pool fraction	CC	-0.015	0.920
		CG	0.012	0.933
		ILF	0.003	0.985
		SLF	0.000	0.997
Free T4	Fractional anisotropy	CC	-0.146	0.227
		CG	0.107	0.375
		ILF	0.056	0.648
		SLF	0.048	0.693
	Mean diffusivity	CC	-0.072	0.573

---

	CG	0.040	0.760
	ILF	-0.054	0.681
	SLF	0.082	0.530
Radial diffusivity	CC	0.010	0.938
	CG	-0.051	0.691
	ILF	-0.043	0.737
	SLF	-0.014	0.912
Bound pool fraction	CC	0.074	0.608
	CG	0.159	0.266
	ILF	0.071	0.629
	SLF	0.116	0.416

---

Table S2. Relationship between ADHD symptoms and white matter tissue microstructure. CC: corpus callosum; CG: cingulum; ILF: inferior longitudinal fasciculus; SLF: superior longitudinal fasciculus. P values are uncorrected for multiple comparisons.

Measurement	Microstructural metric	Tract	Spearman's rho	P value
Impulsivity	Fractional anisotropy	CC	<b>-0.290</b>	<b>0.015</b>
		CG	-0.049	0.683
		ILF	0.148	0.221
		SLF	-0.216	0.073
	Mean diffusivity	CC	0.177	0.166
		CG	0.101	0.441
		ILF	0.169	0.193
		SLF	0.141	0.280
	Radial diffusivity	CC	0.239	0.061
		CG	0.135	0.292
		ILF	0.093	0.469
		SLF	0.190	0.135
	Bound pool fraction	CC	0.125	0.386
		CG	0.134	0.349
		ILF	0.209	0.150
		SLF	0.128	0.370
Inattention	Fractional anisotropy	CC	-0.076	0.533
		CG	0.093	0.443
		ILF	0.108	0.374
		SLF	-0.144	0.234
	Mean diffusivity	CC	0.047	0.716
		CG	0.012	0.930
		ILF	0.110	0.398
		SLF	0.073	0.574
	Radial diffusivity	CC	0.051	0.696
		CG	0.043	0.737
		ILF	0.058	0.650
		SLF	0.138	0.279
	Bound pool fraction	CC	0.171	0.235
		CG	0.229	0.106
		ILF	0.245	0.089
		SLF	0.230	0.104
Overactivity	Fractional anisotropy	CC	-0.223	0.064
		CG	-0.051	0.672
		ILF	0.129	0.288
		SLF	-0.133	0.274

	Mean diffusivity	CC	0.212	0.096
		CG	0.147	0.264
		ILF	<b>0.287</b>	<b>0.025</b>
		SLF	0.190	0.143
	Radial diffusivity	CC	0.228	0.074
		CG	0.187	0.141
		ILF	0.190	0.136
		SLF	0.228	0.072
	Bound pool fraction	CC	0.162	0.261
		CG	0.186	0.191
		ILF	0.204	0.160
		SLF	0.143	0.317
ADHD total score	Fractional anisotropy	CC	-0.170	0.159
		CG	0.054	0.654
		ILF	0.139	0.253
		SLF	-0.177	0.144
	Mean diffusivity	CC	0.168	0.189
		CG	0.117	0.374
		ILF	0.210	0.105
		SLF	0.161	0.215
	Radial diffusivity	CC	0.175	0.173
		CG	0.132	0.303
		ILF	0.118	0.356
		SLF	0.208	0.102
	Bound pool fraction	CC	0.157	0.276
		CG	0.207	0.144
		ILF	0.259	0.073
		SLF	0.189	0.185

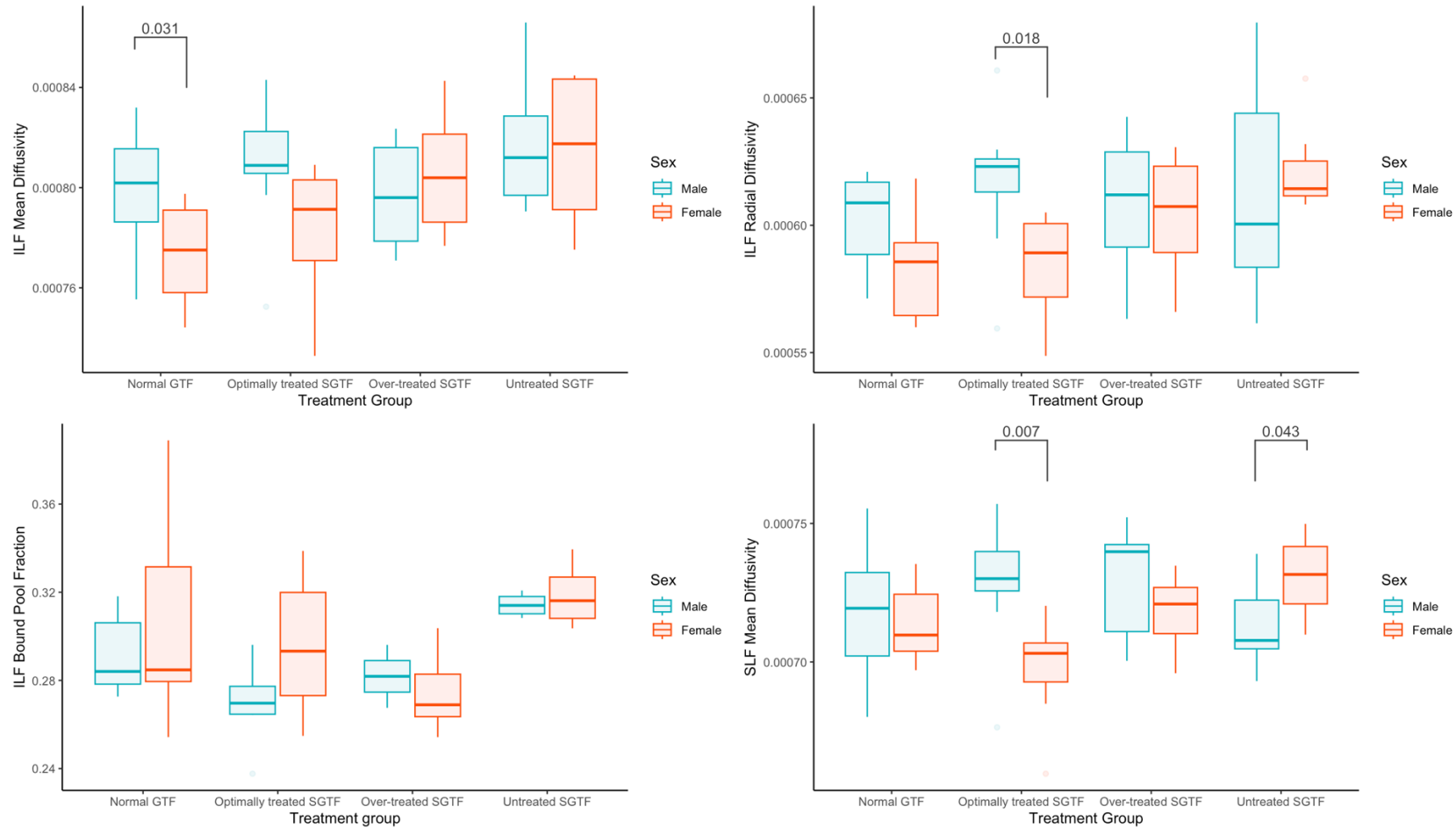
Table S3. Results of regression analyses investigating the effects of treatment group, sex and their interaction on microstructural metrics. CC: corpus callosum; CG: cingulum; ILF: inferior longitudinal fasciculus; SLF: superior longitudinal fasciculus; FDR: False discovery rate.

<b>Metric</b>	<b>Tract</b>	<b>F statistic</b>	<b>Uncorrected p value</b>	<b>FDR-corrected p value</b>
Fractional anisotropy	CC	0.990	0.447	0.596
	CG	1.540	0.170	0.302
	ILF	1.519	0.177	0.283
	SLF	1.780	0.107	0.245
Mean diffusivity	CC	1.989	0.072	0.192
	CG	1.152	0.346	0.503
	ILF	<b>3.234</b>	<b>0.006</b>	0.096
	SLF	<b>2.743</b>	<b>0.016</b>	0.128
Radial diffusivity	CC	1.597	0.155	0.310
	CG	0.622	0.735	0.735
	ILF	<b>2.335</b>	<b>0.036</b>	0.192
	SLF	2.023	0.068	0.218
Bound pool fraction	CC	0.719	0.657	0.701
	CG	0.928	0.494	0.608
	ILF	<b>2.361</b>	<b>0.039</b>	0.156
	SLF	0.731	0.647	0.739

Table S4. Results of post-hoc *t* tests comparing microstructural metrics between male and female participants within each treatment group demonstrating an uncorrected statistical effect in the regression analyses (Table S3). CC: corpus callosum; CG: cingulum; ILF: inferior longitudinal fasciculus; SLF: superior longitudinal fasciculus; FDR: False discovery rate; GTF: gestational thyroid function; SGTF: suboptimal gestational thyroid function.

Metric	Tract	Treatment Group	t value	Uncorrected p value	FDR-corrected p value
Mean diffusivity	ILF	Normal GTF	<b>2.419</b>	<b>0.031</b>	0.165
		Optimally treated SGTF	1.966	0.069	0.221
		Over-treated SGTF	-0.637	0.539	0.862
		Untreated SGTF	0.069	0.946	0.946
	SLF	Normal GTF	0.340	0.74	0.987
		Optimally treated SGTF	<b>3.127</b>	<b>0.007</b>	0.112
		Over-treated SGTF	1.076	0.306	0.699
		Untreated SGTF	<b>-2.240</b>	<b>0.043</b>	0.172
Radial diffusivity	ILF	Normal GTF	0.107	0.917	0.978
		Optimally treated SGTF	<b>2.664</b>	<b>0.018</b>	0.144
		Over-treated SGTF	0.335	0.743	0.914
		Untreated SGTF	-1.215	0.245	0.653
Bound pool fraction	ILF	Normal GTF	0.540	0.597	0.868
		Optimally treated SGTF	-0.819	0.426	0.757
		Over-treated SGTF	-0.945	0.406	0.812
		Untreated SGTF	0.234	0.826	0.944

Figure S1. Boxplots of male and female values for microstructural metrics that demonstrated (uncorrected) significant effects in multiple regressions with interaction effects (treatment group\*sex) from Table S3. *P* values are for post-hoc *t* tests and are uncorrected for multiple comparisons. False-discovery rate-corrected *p* values are available in Table S4. ILF: Inferior longitudinal fasciculus; SLF: Superior longitudinal fasciculus; GTF: gestational thyroid function; SGTF: suboptimal gestational thyroid function.



## References

1. Griswold MA, Jakob PM, Heidemann RM, et al. Generalized autocalibrating partially parallel acquisitions (GRAPPA). *Magn Reson Med*. 2002;47:1202–1210.
2. Mougín OE, Coxon RC, Pitiot A, Gowland PA. Magnetization transfer phenomenon in the human brain at 7T. *Neuroimage* 2010;49(1):272-281.
3. Cercignani M, Symms MR, Schmierer K, et al. Three-dimensional quantitative magnetisation transfer imaging of the human brain. *Neuroimage* 2005;27:436-441.
4. Cercignani M, Alexander DC. Optimal acquisition schemes for in vivo quantitative magnetization transfer MRI. *Magn Reson Med* 2006;56(4):803-810.
5. Jenkinson M, Beckmann CF, Behrens TEJ, Woolrich MW, Smith SM. FSL. *Neuroimage* 2012;62(2):782-790.
6. Isensee F, Schell M, Pflueger I, et al. Automated brain extraction of multisequence MRI using artificial neural networks. *Hum brain mapp* 2019;40(17):4952-4964.
7. Tustison NJ, Avants BB, Cook PA, et al. N4ITK: improved N3 bias correction. *IEEE trans med imaging* 2010;29(6):1310–1320.
8. Stollberger R, Wach P. Imaging of the active B1 field in vivo. *Magn reson med*. 1996;35(2):246–251.
9. Jenkinson M, Smith S. A global optimisation method for robust affine registration of brain images. *Med Image Anal* 2001;5(2):143-156.
10. Jenkinson M, Bannister P, Brady M, Smith S. Improved Optimisation for the Robust and Accurate Linear Registration and Motion Correction of Brain Images. *NeuroImage* 2002;17(2):825-841.
11. Venkatesan R, Lin W, Haacke EM. Accurate determination of spin-density and T1 in the presence of RF-field inhomogeneities and flip-angle miscalibration. *Magn Reson Med* 1998;40:592-602.
12. Zhang Y, Brady M, Smith S. Segmentation of brain MR images through a hidden Markov random field model and the expectation-maximization algorithm. *IEEE Trans Med Imag*, 2001;20(1):45-57,